Sparse Methods for Quantitative Susceptibility Mapping

Berkin Bilgic*[a], Itthi Chatnuntawech[b], Christian Langkammer[c], Kawin Setsompop[a]

[a] Martinos Center for Biomedical Imaging, Charlestown, MA, USA; [b] Massachusetts Institute of Technology, Cambridge, MA, USA, [c] Department of Neurology, Medical University of Graz, Graz, Austria

ABSTRACT

Quantitative Susceptibility Mapping (QSM) aims to estimate the tissue susceptibility distribution that gives rise to subtle changes in the main magnetic field, which are captured by the image phase in a gradient echo (GRE) experiment. The underlying susceptibility distribution is related to the acquired tissue phase through an ill-posed linear system. To facilitate its inversion, spatial regularization that imposes sparsity or smoothness assumptions can be employed. This paper focuses on efficient algorithms for regularized QSM reconstruction. Fast solvers that enforce sparsity under Total Variation (TV) and Total Generalized Variation (TGV) constraints are developed using Alternating Direction Method of Multipliers (ADMM). Through variable splitting that permits closed-form iterations, the computation efficiency of these solvers are dramatically improved. An alternative approach to improve the conditioning of the ill-posed inversion is to acquire multiple GRE volumes at different head orientations relative to the main magnetic field. The phase information from such multi-orientation acquisition can be combined to yield exquisite susceptibility maps and obviate the need for regularized reconstruction, albeit at the cost of increased data acquisition time. Matlab code and data implementing the presented results are available at martinos.org/~berkin/ADMM_QSM.zip

Keywords: MRI, QSM, GRE, phase, sparsity, regularization, TV, TGV

1. INTRODUCTION

The ability to detect tissue anatomy using Magnetic Resonance Imaging (MRI) is limited by the contrast-to-noise ratio (CNR), which depends on the contrast mechanism and the spatial resolution. By exploiting the MRI signal phase as a source of contrast, large increases in CNR can be achieved over conventional magnitude-based MRI techniques (1). Despite the dramatic improvement in anatomic detail, phase images suffer from non-local effects that depend on the geometry and orientation of the tissue (2,3). Quantitative Susceptibility Mapping (QSM) estimates the underlying tissue magnetic susceptibility that gives rise to the phase signal, resolves such geometry dependence, and provides quantitative and exquisite contrast between or even within anatomical structures (4–11). Major sources of susceptibility contrast include tissue iron, calcium, lipid, protein and myelin content. Abnormally high iron deposition in deep gray matter structures is indicative of several neurological diseases as well as aging, and is readily quantified using QSM (12–14). Since deoxygenated blood becomes more paramagnetic, QSM also lends itself to estimation of vessel oxygenation, which can provide assessment of changes in physiology (15–17). For white matter structures, the microscopic composition of the tissue leads to anisotropic susceptibility, which can be characterized using Susceptibility Tensor Imaging (STI) (18–22). As such, magnetic susceptibility emerges as a powerful mechanism that provides quantitative, local and superb tissue contrast with the ability to reveal white matter connectivity of the brain.

The workhorse data acquisition protocol for QSM is the gradient recalled echo (GRE) sequence. The local differences in the magnetic susceptibility of the tissue lead to a subtle perturbation in the MRI magnetic field, which in turn causes the magnetic spins to rotate at different speeds. This subtle difference is captured in the phase of the complex GRE images. High-resolution phase images obtained from GRE acquisition have demonstrated strong contrast between and within gray and white matter. This contrast boost yields almost a 10-fold improvement over conventional magnitude imaging (1). Clinical use of phase images, however, is limited because phase information is not spatially localized, but results from the convolution of the underlying susceptibility distribution with a dipole kernel (23). This also causes phase contrast to be dependent on the head orientation relative to the scanner's main magnetic field. The misleading contrast makes it difficult to relate features in the phase images to the underlying anatomical structures (3,24).

* berkin@nmr.mgh.harvard.edu; martinos.org/~berkin

Wavelets and Sparsity XVI, edited by Manos Papadakis, Vivek K. Goyal, Dimitri Van De Ville,
Proc. of SPIE Vol. 9597, 959711 · © 2015 SPIE · CCC code: 0277-786X/15/$18
doi: 10.1117/12.2188535

Nonetheless, the deconvolution of phase data using QSM overcomes the misleading non-local bias and yields a local tissue property. While QSM provides a quantitative measure of tissue susceptibility, it entails the solution of an ill-posed inverse problem, which requires whole-brain deconvolution of the phase signal and necessitates regularized reconstruction. Such regularization imposes prior assumption on the susceptibility distribution to improve conditioning of the inverse problem. A common prior in QSM is that, magnetic susceptibility is tied to the underlying tissue; hence it should vary smoothly within tissue boundaries. To reflect this assumption, ℓ_2- or ℓ_1- regularization is applied on the image gradients of the susceptibility map during reconstruction. While ℓ_2 penalty promotes a smooth image, ℓ_1 penalty on the gradients (i.e. Total Variation (TV)), enforces a piecewise constant reconstruction. These regularized QSM techniques are commonly known as MEDI (Morphology Enabled Dipole Inversion) (5,6,11), and have proven to be effective for solution of the inverse problem.

A more advanced regularizer is the Total Generalized Variation (TGV), which is an extension of the TV model to higher order image gradients (25,26). TGV relaxes the piecewise constant image assumption of the TV model to promote a piecewise smooth reconstruction. This is a more natural prior for medical images that also mitigates the staircasing artifact TV suffers from. TGV has recently been extended to QSM (27,28), and provided a viable alternative to TV regularization.

An alternative way to improve conditioning of the dipole inversion is to acquire additional GRE images at different head orientations relative to the MRI magnetic field. As the patients move their head to a new position inside the scanner, the dipole kernel that explains the convolution operation is also rotated. As such, collecting phase data at multiple orientations and combining them during QSM reconstruction is an effective way of mitigating the ill-posedness of the inversion. Multi-orientation QSM obviates the need for additional regularization, and provides exquisite tissue contrast. This technique is known as Calculation Of Susceptibility through Multiple Orientation Sampling (COSMOS) (4,5,8,9,29). The disadvantage of COSMOS is the increased data sampling requirement, which leads to substantially lengthened acquisition times at less natural head positions.

In this paper, we review fast algorithms for ℓ_2- and ℓ_1- regularized QSM (30,31). In particular, we present a closed-form solution for the ℓ_2-constrained inversion, and employ Alternating Direction Method of Multipliers (ADMM) (32,33) to efficiently solve the TV-regularized problem. ADMM separates the TV optimization problem into simpler sub-problems, which can be solved efficiently in closed-form. For the first time, we also demonstrate closed-form iterations for TGV-regularized QSM with the ADMM formalism. We conclude with a comparison between regularized QSM from single-orientation and multi-orientation QSM.

Accompanying data and Matlab software can be downloaded from martinos.org/~berkin/ADMM_QSM.zip

2. REGULARIZED QSM FROM SINGLE-ORIENTATION ACQUISITION

2.1 Closed-form reconstruction for ℓ_2-regularized QSM

The tissue phase ϕ obtained from the GRE experiment is related to the unknown susceptibility map χ via the linear relation $\mathbf{F}^H\mathbf{D}\mathbf{F}\chi = \phi$, where $\mathbf{F}$ is the discrete Fourier transform (DFT) operator, and the diagonal matrix $\mathbf{D} = (1/3 - k_z^2/k^2)$ is the dipole kernel. This kernel undersamples the frequency content of χ in the vicinity of the "magic angle", given by the double-conical surface defined by $3k_z^2 = k^2$, where $k = (k_x, k_y, k_z)$ is the frequency index. The tissue phase ϕ is obtained by unwrapping the raw phase from the GRE data (2,34), followed by background phase removal (7,10). To mitigate the undersampling artifacts, the following ℓ_2-regularized reconstruction can be considered:

$$min_\chi \frac{1}{2}\|\mathbf{F}^H\mathbf{D}\mathbf{F}\chi - \phi\|_2^2 + \frac{\beta}{2}\|\mathbf{G}\chi\|_2^2 \quad (1)$$

Here, $\mathbf{G}$ is the image gradient operator in 3-dimensions, and β is a regularization parameter controlling the amount of prior information to be introduced. The gradient operator can be decomposed as $\mathbf{G} = \mathbf{F}^H\mathbf{E}\mathbf{F}$, where E is a diagonal matrix that represents a phase ramp in frequency space to implement the differencing operation. With this decomposition, the solution of Eq.1 is found by taking the derivative and setting it to zero:

$$\mathbf{F}^H(\mathbf{D}^H\mathbf{D} + \beta\mathbf{E}^H\mathbf{E})\mathbf{F}\chi = \mathbf{F}^H\mathbf{D}^H\mathbf{F}\phi \quad (2)$$

The optimizer can then be computed in closed-form (30),

$$\chi = \mathbf{F}^H(\mathbf{D}^H\mathbf{D} + \beta\mathbf{E}^H\mathbf{E})^{-1}\mathbf{D}^H\mathbf{F}\phi \tag{3}$$

Since the matrix inversion involves only diagonal matrices, it is trivial to compute. The computational requirement of closed-form ℓ_2 solution is just two DFT evaluations and element-wise multiplications.

2.2 Closed-form iterations for TV-regularized QSM using ADMM

For TV-regularized QSM, the optimization problem becomes

$$\min_{\chi} \frac{1}{2}\|\mathbf{F}^H\mathbf{D}\mathbf{F}\chi - \phi\|_2^2 + \alpha_1\|\mathbf{G}\chi\|_1 \tag{4}$$

We adopt the ADMM formalism and introduce additional variables z_1 and s_1 (31),

$$\min_{\chi,z_1} \frac{1}{2}\|\mathbf{F}^H\mathbf{D}\mathbf{F}\chi - \phi\|_2^2 + \alpha_1\|z_1\|_1 + \frac{\mu_1}{2}\|\mathbf{G}\chi - z_1 + s_1\|_2^2 \tag{5}$$

Here z_1 is an auxiliary variable representing the gradient of the susceptibility map and s_1 is the scaled Lagrange multiplier. We separate this optimization into subproblems and optimize with respect to each of the unknown variables sequentially while keeping the other two constant. The subproblem for χ is,

$$\min_{\chi} \frac{1}{2}\|\mathbf{F}^H\mathbf{D}\mathbf{F}\chi - \phi\|_2^2 + \frac{\mu_1}{2}\|\mathbf{G}\chi - z_1 + s_1\|_2^2 \tag{6}$$

This expression is very similar to Eq.1 and can be similarly solved in closed-form,

$$\chi = \mathbf{F}^H(\mathbf{D}^H\mathbf{D} + \mu_1\mathbf{E}^H\mathbf{E})^{-1}[\mathbf{D}^H\mathbf{F}\phi + \mu_1\mathbf{E}^H\mathbf{F}(z_1 - s_1)] \tag{7}$$

The subproblem for z_1 update is,

$$\min_{z_1} \alpha_1\|z_1\|_1 + \frac{\mu_1}{2}\|\mathbf{G}\chi - z_1 + s_1\|_2^2 \tag{8}$$

This also admits a closed-form solution through the soft thresholding operation,

$$z_1 = \max(|\mathbf{G}\chi + s_1| - \alpha_1/\mu_1, 0) \cdot sign(\mathbf{G}\chi + s_1) \tag{9}$$

Finally, the update rule for the Lagrange multiplier is given by

$$s_1 = s_1 + \mathbf{G}\chi - z_1 \tag{10}$$

The TV ADMM algorithm is then the application of closed-form update rules Eqs.7, 9 and 10 until a convergence criterion is satisfied.

2.3 Closed-form iterations for TGV-regularized QSM using ADMM

The extension to the second order TGV regularization involves solving,

$$\min_{\chi,v} \frac{1}{2}\|\mathbf{F}^H\mathbf{D}\mathbf{F}\chi - \phi\|_2^2 + \alpha_1\|\mathbf{G}\chi - v\|_1 + \alpha_0\|\boldsymbol{\mathcal{E}}v\|_1 \tag{11}$$

where $\boldsymbol{\mathcal{E}}$ is the symmetrized gradient operator (25,28). We introduce additional variables to revert to ADMM formalism,

$$\min_{\chi,v,z_1,z_0} \frac{1}{2}\|\mathbf{F}^H\mathbf{D}\mathbf{F}\chi - \phi\|_2^2 + \alpha_1\|z_1\|_1 + \frac{\mu_1}{2}\|\mathbf{G}\chi - v - z_1 + s_1\|_2^2 + \alpha_0\|z_0\|_1 + \frac{\mu_0}{2}\|\boldsymbol{\mathcal{E}}v - z_0 + s_0\|_2^2 \tag{12}$$

The subproblem that needs to be solved for the (χ, v) pair is

$$\min_{\chi,v} \frac{1}{2}\|\mathbf{F}^H\mathbf{D}\mathbf{F}\chi - \phi\|_2^2 + \frac{\mu_1}{2}\|\mathbf{G}\chi - v - z_1 + s_1\|_2^2 + \frac{\mu_0}{2}\|\boldsymbol{\mathcal{E}}v - z_0 + s_0\|_2^2 \tag{13}$$

Taking the gradient of Eq.13 with respect to both χ and v yields the following system of linear equations

$$\begin{bmatrix} \mathbf{F}^H\mathbf{D}^H\mathbf{D}\mathbf{F} + \mu_1\mathbf{G}^H\mathbf{G} & -\mu_1\mathbf{G}^H \\ -\mu_1\mathbf{G} & \mu_1\mathbf{I} + \mu_0\boldsymbol{\mathcal{E}}^H\boldsymbol{\mathcal{E}} \end{bmatrix} \begin{bmatrix} \chi \\ v \end{bmatrix} = \begin{bmatrix} \mathbf{F}^H\mathbf{D}^H\mathbf{F}\phi + \mu_1\mathbf{G}^H(z_1 - s_1) \\ \mu_0\boldsymbol{\mathcal{E}}^H(z_0 - s_0) - \mu_1(z_1 - s_1) \end{bmatrix} \tag{14}$$

which can be diagonalized by DFT and yield

$$\begin{bmatrix} \mathbf{D}^H\mathbf{D} + \mu_1\mathbf{E}^H\mathbf{E} & -\mu_1\mathbf{E}^H \\ -\mu_1\mathbf{E} & \mu_1\mathbf{I} + \mu_0\boldsymbol{\Sigma}^H\boldsymbol{\Sigma} \end{bmatrix} \begin{bmatrix} \mathbf{F}\chi \\ \mathbf{F}v \end{bmatrix} = \begin{bmatrix} \mathbf{D}^H\mathbf{F}\phi + \mu_1\mathbf{E}^H\mathbf{F}(z_1 - s_1) \\ \mu_0\boldsymbol{\Sigma}^H\mathbf{F}(z_0 - s_0) - \mu_1\mathbf{F}(z_1 - s_1) \end{bmatrix} \quad (15)$$

with $\boldsymbol{\mathcal{E}} = \mathbf{F}^H\boldsymbol{\Sigma}\mathbf{F}$. Moreover, a simple reordering of the resulting system of equations results in a block-diagonal structure with each block being a 4 × 4 Hermitian positive-definite matrix. As a result, we can easily update each voxel of $(\mathbf{F}\chi, \mathbf{F}v)$ using a direct inversion of these 4 × 4 blocks. Please refer to the accompanying Matlab code for implementation details of this closed-form inversion.

z_1 and z_0 are updated using soft thresholding operations,

$$z_1 = \max\left(|\mathbf{G}\chi - v + s_1| - \alpha_1/\mu_1, 0\right) \cdot sign(\mathbf{G}\chi - v + s_1) \quad (16)$$
$$z_0 = \max\left(|\boldsymbol{\mathcal{E}}v + s_0| - \alpha_0/\mu_0, 0\right) \cdot sign(\boldsymbol{\mathcal{E}}v + s_0) \quad (17)$$

Finally, the update rules for the Lagrange multipliers are,

$$s_1 = s_1 + \mathbf{G}\chi - v - z_1 \quad (18)$$
$$s_0 = s_0 + \boldsymbol{\mathcal{E}}v - z_0 \quad (19)$$

The overall TGV ADMM algorithm is then the iterative application of the solution of Eq.15 and Eqs.16-19.

3. COSMOS QSM FROM MULTI-ORIENTATION ACQUISITION

As the imaged object is rotated with respect to the main MRI magnetic field, the dipole convolution relating the acquired phase ϕ_i to the susceptibility distribution χ becomes $\phi_i = \mathbf{F}^H\mathbf{D}_i\mathbf{F}\chi$, where i is the orientation index and $\mathbf{D}_i$ denotes the dipole kernel in the i^{th} frame due to $\mathbf{D}_i = 1/3 - k_{zi}^2/k^2$. The index k_{zi} is the projection of the k-space vector in the i^{th} frame onto the main MRI field direction. The collection of phase images at N orientations can be formatted to yield the over-determined system,

$$\begin{bmatrix} \mathbf{D}_1 \\ \vdots \\ \mathbf{D}_N \end{bmatrix} \mathbf{F}\chi = \begin{bmatrix} \mathbf{F}\phi_1 \\ \vdots \\ \mathbf{F}\phi_N \end{bmatrix} \quad (20)$$

This set of equations can be solved in the least-squares sense by considering the problem

$$\min_{\chi} \sum_{i=1}^{N} \|\mathbf{D}_i\mathbf{F}\chi - \mathbf{F}\phi_i\|_2^2 \quad (21)$$

Taking the gradient of Eq.21 and setting it to zero yields a closed-form solution,

$$\chi_{cosmos} = \mathbf{F}^H\left(\sum_{i=1}^{N}\mathbf{D}_i^H\mathbf{D}_i\right)^{-1}\sum_{i=1}^{N}\mathbf{D}_i^H\mathbf{F}\phi_i \quad (22)$$

This solution requires only DFT evaluations, point-wise multiplications, and the inversion of a diagonal matrix. It is thus extremely efficient, usually requiring several seconds of computation.

4. EXPERIMENTAL EVALUATION

4.1 Numerically simulated phantom

A numerical susceptibility phantom was adapted from (22,28) to compare QSM reconstruction performance of closed-form ℓ_2, TV ADMM and TGV ADMM algorithms (Fig.1). This phantom was created by segmentation of a brain into white matter, gray matter and cerebrospinal fluid (CSF). Susceptibilities were set to similar values observed in vivo: CSF = 0 ppm, globus pallidus = 0.19 ppm, putamen = 0.09 ppm, thalamus = 0.07 ppm, red nucleus = 0.07 ppm, substantia nigra = 0.09 ppm, dentate nucleus = 0.09 ppm, caudate nucleus = 0.09 ppm, and cortical gray matter = 0.05 ppm. Susceptibilities of white matter structures ranged from –0.03 to –0.01 ppm. Geometric properties were, matrix size = 256 × 256 × 98, and resolution = 0.94 × 0.94 × 1.5 mm^3. A smoothly varying susceptibility ramp was added inside the thalamus to better emulate in vivo susceptibility distribution. This phantom was convolved with the dipole kernel to simulate the phase data and white Gaussian noise was added to incur 25.2% root mean square error (RMSE) relative to the noiseless phase.

Regularization parameters for closed-form ℓ_2 and TV ADMM that minimized RMSE were $\beta = 3 \cdot 10^{-3}$ and $(\alpha_1 = 2 \cdot 10^{-4}, \mu_1 = 10^{-2})$. To simplify parameter selection, the same α_1 and μ_1 values were used for TGV ADMM,

and μ_0 was set equal to μ_1. The best RMSE was obtained using $\alpha_0 = 2\alpha_1$. The convergence criterion to stop TV and TGV iterations was achieving less than 1% change in the susceptibility estimates between successive iterations. With this setting, the reconstruction errors were 33.5%, 19.6% and 19.9% for ℓ_2-, TV- and TGV-regularized QSM (Fig.1). Despite similar RMSE performance, TGV reconstruction was able to mitigate the staircasing artifact present in the TV solution of the thalamus (Fig.1 lower panel). The processing times were 0.3 sec for closed-form ℓ_2, 10 sec for TV ADMM and 25 sec for TGV ADMM on a workstation with 32 processors and 192 GB memory.

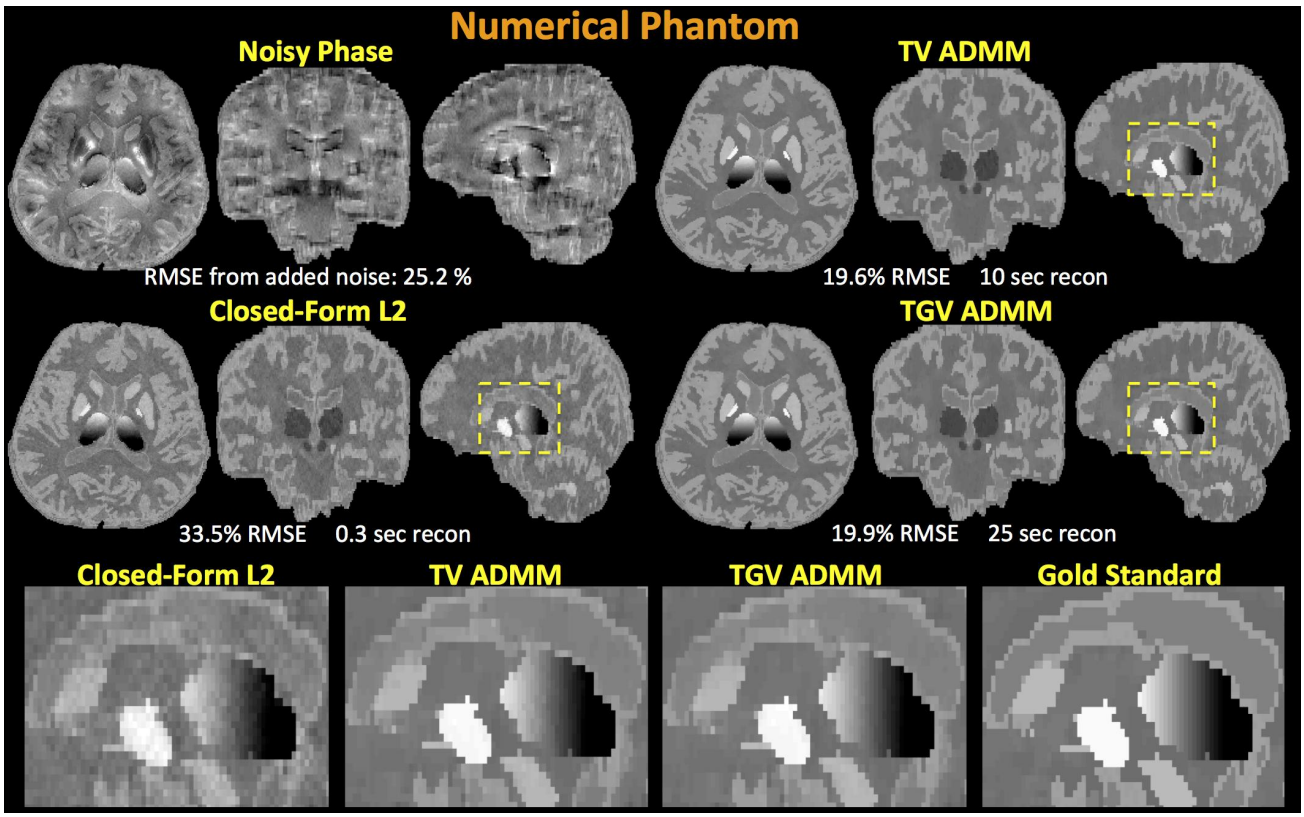

Figure 1. QSM reconstruction results for the numerically simulated phantom. TV and TGV priors were more successful than the closed-form solution in mitigating the reconstruction artifacts, while TGV had also the ability of preserving the smooth variation inside the thalamus.

4.2 Simulated phantom from in vivo COSMOS acquisition

To obtain an in vivo gold standard susceptibility map, a healthy volunteer was scanned at 3T to sample 12 different head orientations. Highly accelerated (R=15) 3D-GRE with Wave-CAIPI sequence was utilized to facilitate data acquisition, which took 90 sec per head orientation (29,35). The voxel size was 1.1 mm isotropic at repetition time (TR) / echo time (TE) = 35/25 msec. Following brain masking using FSL BET (36) and registration onto the neutral head position using FSL FLIRT (37), the phase image from each orientation was unwrapped and the background field was removed (2,10). Using the orientation information from the registration step, COSMOS solution was obtained from Eq.22.

Tissue phase was simulated by convolving this gold standard COSMOS susceptibility with the dipole kernel and white Gaussian noise was added to incur 19.7% RMSE relative to the noiseless phase. The optimal parameter setting that minimized the QSM reconstruction error was $\beta = 2 \cdot 10^{-3}$, $(\alpha_1 = 5 \cdot 10^{-5}, \mu_1 = 2 \cdot 10^{-3})$ and $\alpha_0 = \alpha_1/3$. To simplify parameter selection for TGV ADMM, the same α_1 and μ_1 values as TV ADMM were used, and μ_0 was set equal to μ_1. The reconstruction errors were 30.1%, 26.3%, and 25.1% for the ℓ_2-, TV- and TGV-regularized QSM (Fig.2). The computation times were 0.2, 5 and 14 sec for the three algorithms. TGV reconstruction was able to obtain the lowest

reconstruction error, while also mitigating subtle staircasing artifacts that were present in the TV solution (white arrow in Fig.2 lower panel).

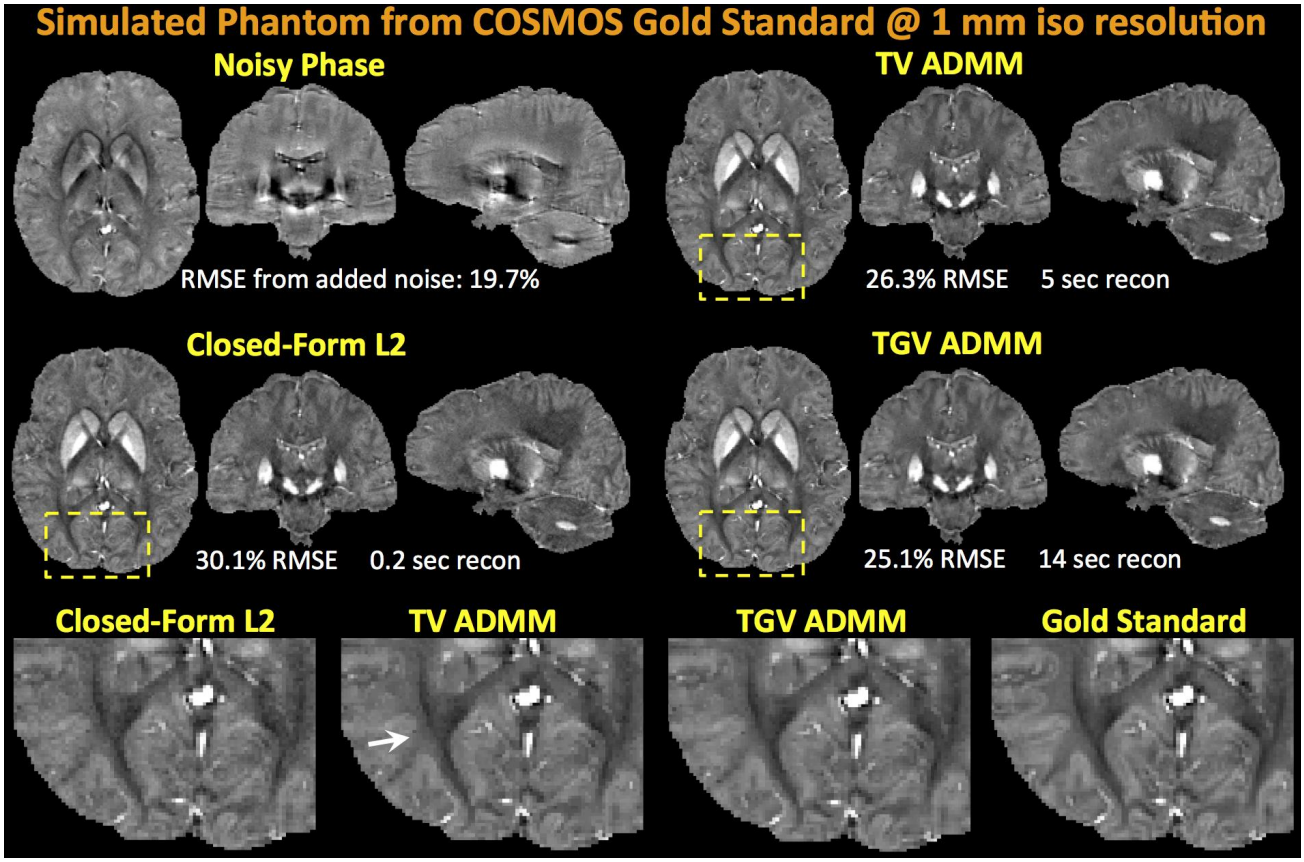

Figure 2. QSM reconstructions using phase data simulated from gold standard in vivo COSMOS susceptibility. TGV ADMM achieves the best performance as measured by RMSE, and mitigates subtle staircasing artifacts present in the TV reconstruction (white arrow in lower panel).

4.3 In vivo GRE acquisition at 0.6 mm isotropic resolution at single-orientation

High resolution 3D-GRE data acquired on a healthy volunteer at 3T (31) were used to provide in vivo comparison between the three QSM algorithms. Imaging parameters were as follows: 0.6 mm isotropic resolution, TR/TE = 26/8.1 msec, matrix size = 384×336×224, GRAPPA acceleration factor = 2, phase partial Fourier = 75%, and acquisition time = 15 min 42 sec. Tissue phase was obtained using a processing pipeline consisting of brain extraction with FSL BET (36), Laplacian phase unwrapping (2,34), and SHARP background removal (7). Parameter selection was guided by L-curve analysis, and the selected parameters were $\beta = \mu_1 = 3 \cdot 10^{-2}$, and $\alpha_1 = 6 \cdot 10^{-4}$. The second order regularization parameter α_0 was set to $\alpha_0 = 2\alpha_1$.

For this high resolution dataset, the reconstruction times were 1, 48 and 180 sec for the ℓ_2-, TV- and TGV-regularized algorithms (Fig.3). TV and TGV ADMM solutions had similar quality, and were able to mitigate the frequency undersampling effect along the magic angle more effectively than the closed-form ℓ_2 solution (Fig.3 lower panel).

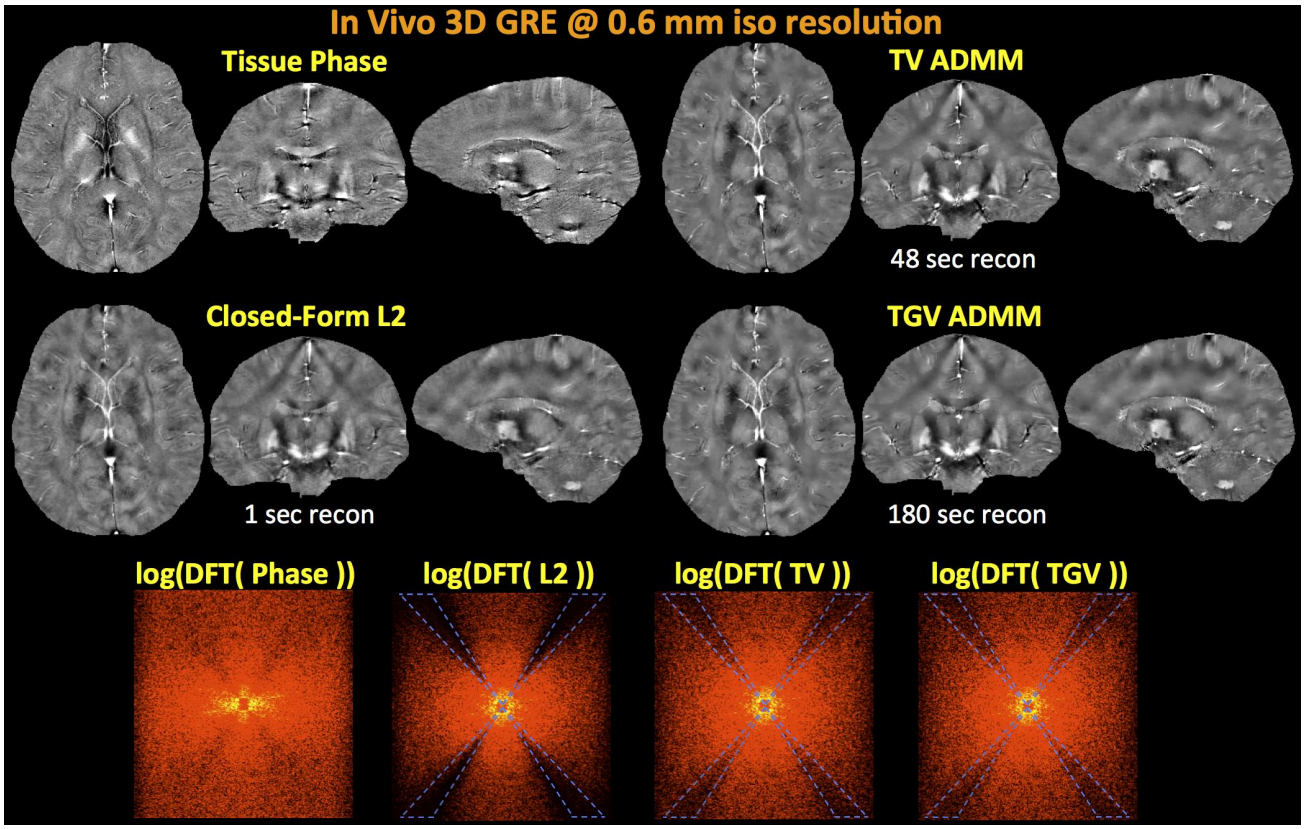

Figure 3. In vivo susceptibility mapping with 0.6 mm isotropic resolution at 3T. TV and TGV reconstructions are more successful than the ℓ_2 penalty at mitigating the frequency undersampling along the magic angle (dashed triangles).

4.4 In vivo GRE acquisition at 1 mm isotropic resolution at multi-orientation

Finally, to provide comparison between multi-orientation COSMOS and single-orientation TV ADMM solutions, in vivo 3D-GRE data were acquired at 3 different head positions at 3T. The acquisition parameters were, FOV=240×240×192 mm^3, TR/TE = 40/30 msec, 1 mm^3 resolution, R=9 fold acceleration with Wave-CAIPI, total scan time = 10.3 min. Phase data from each orientation went through BET brain masking, Laplacian unwrapping and SHARP filtering, followed by FLIRT registration onto the neutral head position frame. Multi-orientation data were combined using Eq.22 to create COSMOS susceptibility maps, while TV ADMM reconstruction was applied on the single-orientation phase data at the neutral head position (Fig.4).

Compared to the COSMOS reconstruction that provides exquisite data quality, TV ADMM solution introduces some smoothing while mitigating the streaking artifacts due to undersampling (Fig.4). Compared to the single-orientation acquisition that was completed in 3.5 min, multi-orientation sampling at three positions required 10.3 min. As such, the improvement in image quality of the COSMOS maps comes at the cost of substantially increased scan time and is also hardly feasible in less compliant patients.

5. CONCLUSION

We have reviewed existing efficient algorithms for ℓ_2- and TV-regularized QSM, and introduced a novel algorithm for TGV-regularized dipole inversion based on ADMM formalism. This variable splitting approach divides the ℓ_1-regularized optimization problem into subproblems that can be solved efficiently in closed-form, leading to dramatic computational savings. In numerical and in vivo experiments, TV and TGV penalties were shown to yield more accurate reconstructions than the ℓ_2 solution, with the ability to compensate the undersampled frequency content of the

susceptibility distribution. While TGV had comparable performance to TV in terms of reconstruction error, it allowed mitigation of staircasing artifacts present in the TV reconstructions. Despite improved image modeling, single-orientation techniques are unable to match the high data quality provided by multi-orientation sampling (8). Regularized QSM at single-orientation relies on prior information to mitigate the streaking artifacts due to undersampling in frequency space, but this in turn introduces a certain amount of smoothing to the final reconstruction. Regularization parameter selection is another drawback of the single-orientation techniques, which is usually performed based on discrepancy principle (38) or L-curve (39) heuristics. A further drawback of the TGV technique is the introduction of two additional parameters, μ_0 and α_0, that control the fidelity and sparsity of the second order gradients. To simplify parameter selection (potentially at the cost of suboptimality), we have chosen to set $\mu_0 = \mu_1$, and used a fixed scaling relation between α_0 and α_1 as suggested in (25,28). Multi-orientation QSM, on the other hand, obviates the need for regularization parameter selection and provides higher quality susceptibility maps without streaking or smoothing artifacts. This comes at the cost of increased scan time, which can be mitigated using efficient acquisition techniques (28,29).

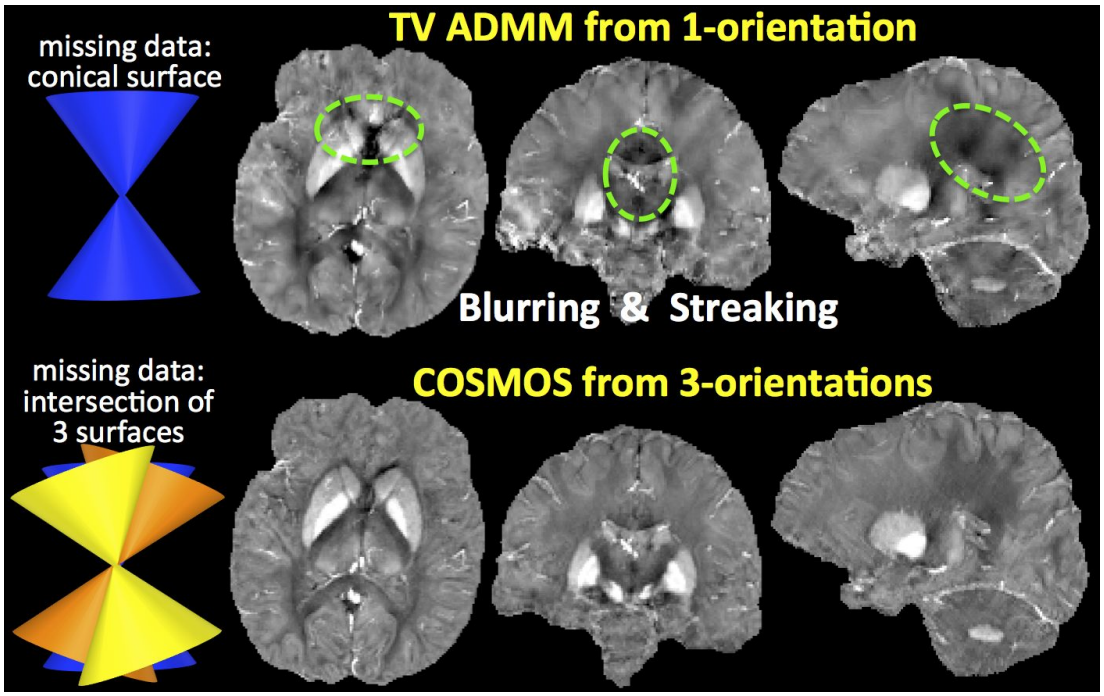

Figure 4. Compared to the TV-regularized QSM from single head orientation, COSMOS reconstruction from 3 orientations yield higher data quality without smoothing or streaking artifacts. This, however, comes at the cost of substantially increased scan time, which can be mitigated using efficient acquisition techniques.

6. ACKNOWLEDGMENT

We gratefully acknowledge support from NIH, grant numbers NIH NIBIB P41-EB015896, 1U01MH093765, R00EB012107, and R24MH106096.

REFERENCES

1. Duyn J, Gelderen P van, Tie-Qiang L, de Zwart JA, Koretsky AP, Fukunaga M. High-field MRI of brain cortical substructure based on signal phase. Proc. Natl. Acad. Sci. 2007;104:11796–11801.
2. Li W, Wu B, Liu C. Quantitative susceptibility mapping of human brain reflects spatial variation in tissue composition. Neuroimage 2011;55:1645–1656.

3. Deistung A, Schäfer A, Schweser F, Biedermann U, Turner R, Reichenbach JR. Toward in vivo histology : A comparison of quantitative susceptibility mapping (QSM) with magnitude-, phase-, and R2*-imaging at ultra-high magnetic field strength. Neuroimage 2013;65:299–314.
4. Liu T, Spincemaille P, de Rochefort L, Kressler B, Wang Y. Calculation of susceptibility through multiple orientation sampling (COSMOS): a method for conditioning the inverse problem from measured magnetic field map to susceptibility source image in MRI. Magn. Reson. Med. 2009;61:196–204.
5. Liu T, Liu J, de Rochefort L, Spincemaille P, Khalidov I, Ledoux JR, Wang Y. Morphology enabled dipole inversion (MEDI) from a single-angle acquisition: comparison with COSMOS in human brain imaging. Magn. Reson. Med. 2011;66:777–83.
6. Liu J, Liu T, de Rochefort L, et al. Morphology enabled dipole inversion for quantitative susceptibility mapping using structural consistency between the magnitude image and the susceptibility map. Neuroimage 2012;59:2560–8.
7. Schweser F, Deistung A, Lehr BW, Reichenbach JR. Quantitative imaging of intrinsic magnetic tissue properties using MRI signal phase: an approach to in vivo brain iron metabolism? Neuroimage 2011;54:2789–807.
8. Wharton S, Bowtell R. Whole-brain susceptibility mapping at high field: a comparison of multiple- and single-orientation methods. Neuroimage 2010;53:515–525.
9. Khabipova D, Wiaux Y, Gruetter R, Marques JP. A modulated closed form solution for quantitative susceptibility mapping--a thorough evaluation and comparison to iterative methods based on edge prior knowledge. Neuroimage 2015;107:163–74. doi: 10.1016/j.neuroimage.2014.11.038.
10. Wu B, Li W, Guidon A, Liu C. Whole brain susceptibility mapping using compressed sensing. Magn. Reson. Med. 2012;67:137–47.
11. De Rochefort L, Liu T, Kressler B, Liu J, Spincemaille P, Lebon V, Wu J, Wang Y. Quantitative susceptibility map reconstruction from MR phase data using bayesian regularization: validation and application to brain imaging. Magn. Reson. Med. 2010;63:194–206.
12. Bilgic B, Pfefferbaum A, Rohlfing T, Sullivan E V, Adalsteinsson E. MRI estimates of brain iron concentration in normal aging using quantitative susceptibility mapping. Neuroimage [Internet] 2012;59:2625–35. doi: 10.1016/j.neuroimage.2011.08.077.
13. Langkammer C, Liu T, Khalil M, Enzinger C, Jehna M, Fuchs S, Fazekas F, Wang Y, Ropele S. Quantitative susceptibility mapping in multiple sclerosis. Radiology 2013;267:551–9. doi: 10.1148/radiol.12120707.
14. Acosta-Cabronero J, Williams G, Cardenas-Blanco A, Arnold RJ, Lupson V, Nestor PJ. In Vivo Quantitative Susceptibility Mapping (QSM) in Alzheimer's Disease. PLoS One 2013;8:e81093.
15. Fan AP, Benner T, Bolar DS, Rosen BR, Adalsteinsson E. Phase-based regional oxygen metabolism (PROM) using MRI. Magn. Reson. Med. 2012;67:669–78. doi: 10.1002/mrm.23050.
16. Fan APA, Bilgic B, Gagnon L, Witzel T, Bhat H, Rosen BR, Adalsteinsson E. Quantitative oxygenation venography from MRI phase. Magn. Reson. Med. [Internet] 2013;72:149–59. doi: 10.1002/mrm.24918.
17. Fan AP, Evans KC, Stout JN, Rosen BR, Adalsteinsson E. Regional quantification of cerebral venous oxygenation from MRI susceptibility during hypercapnia. Neuroimage 2015;104:146–55. doi: 10.1016/j.neuroimage.2014.09.068.
18. Liu C. Susceptibility tensor imaging. Magn. Reson. Med. 2010;63:1471–1477.
19. Liu C, Li W, Wu B, Jiang Y, Johnson GA. 3D fiber tractography with susceptibility tensor imaging. Neuroimage 2012;59:1290–8. doi: 10.1016/j.neuroimage.2011.07.096.
20. Li X, Vikram DSD, Lim IALI, Jones CKC, Farrell J a D, van Zijl PCM. Mapping magnetic susceptibility anisotropies of white matter in vivo in the human brain at 7T. Neuroimage 2012;62:314–330.
21. Li X, van Zijl PCM. Mean magnetic susceptibility regularized susceptibility tensor imaging (MMSR-STI) for estimating orientations of white matter fibers in human brain. Magn. Reson. Med. 2014;72:610–9. doi: 10.1002/mrm.25322.
22. Wisnieff C, Liu T, Spincemaille P, Wang S, Zhou D, Wang Y. Magnetic susceptibility anisotropy: Cylindrical symmetry from macroscopically ordered anisotropic molecules and accuracy of MRI measurements using few orientations. Neuroimage 2013;70C:363–376. doi: 10.1016/j.neuroimage.2012.12.050.
23. Marques JP, Bowtell R. Application of a Fourier-based method for rapid calculation of field inhomogeneity due to spatial variation of magnetic susceptibility. Concepts Magn. Reson. Part B Magn. Reson. Eng. 2005;25B:65–78.
24. Schäfer A, Wharton S, Gowland P, Bowtell R. Using magnetic field simulation to study susceptibility-related phase contrast in gradient echo MRI. Neuroimage 2009;48:126–137.
25. Bredies K, Kunisch K, Pock T. Total Generalized Variation. SIAM J. Imaging Sci. 2010;3:492–526. doi: 10.1137/090769521.

26. Knoll F, Bredies K, Pock T, Stollberger R. Second order total generalized variation (TGV) for MRI. Magn. Reson. Med. 2011;65:480–91. doi: 10.1002/mrm.22595.
27. Yanez F, Fan A, Bilgic B, Milovic C, Adalsteinsson E, Irarrazaval P. Quantitative Susceptibility Map Reconstruction via a Total Generalized Variation Regularization. In: 2013 International Workshop on Pattern Recognition in Neuroimaging. IEEE; 2013. pp. 203–206. doi: 10.1109/PRNI.2013.59.
28. Langkammer C, Bredies K, Poser BA, Barth M, Reishofer G, Fan AP, Bilgic B, Fazekas F, Mainero C, Ropele S. Fast quantitative susceptibility mapping using 3D EPI and total generalized variation. Neuroimage 2015;111:622–30. doi: 10.1016/j.neuroimage.2015.02.041.
29. Bilgic B, Xie L, Dibb R, et al. Rapid Multi-Orientation Quantitative Susceptibility Mapping. Neuroimage 2015. doi: 10.1016/j.neuroimage.2015.08.015.
30. Bilgic B, Chatnuntawech I, Fan A, Setsompop K, Cauley S, Wald L, Adalsteinsson E. Fast image reconstruction with L2-regularization. J. Magn. Reson. Imaging 2014;40:181–191.
31. Bilgic B, Fan AP, Polimeni JR, Cauley SF, Bianciardi M, Adalsteinsson E, Wald LL, Setsompop K. Fast quantitative susceptibility mapping with L1-regularization and automatic parameter selection. Magn. Reson. Med. 2014;72:1444–59.
32. Boyd S, Parikh N, Chu E, Peleato B, Eckstein J. Distributed Optimization and Statistical Learning via the Alternating Direction Method of Multipliers. Found. Trends® Mach. Learn. 2010;3:1–122. doi: 10.1561/2200000016.
33. Goldstein T, Osher S. The split Bregman method for L1-regularized problems. SIAM J. Imaging Sci. 2009;2:323–343.
34. Schofield MA, Zhu Y. Fast phase unwrapping algorithm for interferometric applications. Opt. Lett. 2003;28:1194. doi: 10.1364/OL.28.001194.
35. Bilgic B, Gagoski BA, Cauley SF, Fan AP, Polimeni JR, Grant PE, Wald LL, Setsompop K. Wave-CAIPI for highly accelerated 3D imaging. Magn. Reson. Med. 2015;73:2152–2162.
36. Smith S. Fast robust automated brain extraction. Hum. Brain Mapp. 2002;17:143–155.
37. Jenkinson M, Bannister P, Brady M, Smith S. Improved optimization for the robust and accurate linear registration and motion correction of brain images. Neuroimage 2002;17:825–841.
38. Morozov V. On the solution of functional equations by the method of regularization. Sov. Math. Dokl 1966;7:414–417.
39. Hansen PC. The L-Curve and its Use in the Numerical Treatment of Inverse Problems. WIT Press, Southampton; 2000.